Damping effects on vortex-induced vibration of a circular cylinder and implications for power extraction

Atul Kumar Soti [a,*], Jisheng Zhao [b], Mark C. Thompson [b], John Sheridan [b], Rajneesh Bhardwaj [c]

[a] IITB-Monash Research Academy, IIT Bombay, Mumbai, Maharashtra, 400076, India
[b] Fluids Laboratory for Aeronautical and Industrial Research (FLAIR), Department of Mechanical and Aerospace Engineering, Monash University, Clayton 3800, Australia
[c] Department of Mechanical Engineering, IIT Bombay, Mumbai, Maharashtra, 400076, India

HIGHLIGHTS

- The damping effects on VIV of a circular cylinder were studied experimentally.
- A simple and tuneable eddy-current-based passive damping mechanism was constructed.
- Different VIV response branches of the cylinder are identified at higher damping.
- A fitting is proposed for the peak amplitude data as a function of mass–damping and Re.
- The flow power extraction efficiency of the cylinder is 20% at the highest Re considered.

ARTICLE INFO

ABSTRACT

The effect of damping on vortex-induced vibration (VIV) of a circular cylinder with a fixed mass ratio ($m^* = 3.0$) was studied through water-channel experiments. An eddy-current-based damping mechanism was constructed to provide controlled and adjustable damping values. It consisted of a permanent magnet connected to the cylinder that moves parallel to a copper plate at some predetermined gap, which determines the damping in the system. Increased damping was found to reduce the reduced-velocity range of the upper and lower branches, thus reducing the synchronization region. As the damping is increased, the lower branch remains easy to identify from the amplitude response curves, but the boundary between the initial and upper branch becomes less clear. However, the frequency response under higher damping shows similarities to that at the lowest damping and these similarities, for the first time, were used to delimit the different response branches. The existence of the upper branch was found to continue down to $A^* \approx 0.2D$. The experimental data was assembled to plot the peak amplitude response as a function of the mass–damping parameter in a "Griffin plot". Due to a restricted variation in Reynolds number in the experiments, the measured data shows negligible scatter compared to the assembled literature data. Three sets of experiments using different sets of springs were conducted to quantify the Reynolds number effect previously established by Govardhan and Williamson (2006). An exponential fitting function was then used to successfully fit the data on the Griffin plot. Under higher damping, it was found that the total and vortex phases are no longer at either 0° or 180°, and take intermediate values throughout the response branches. The power extracted by the damping mechanism was also calculated. Maximum power extraction occurs for a combination of optimal damping and reduced velocity. The

---

* Corresponding author.
  E-mail address: atulsoti@gmail.com (A.K. Soti).

power was also found to increase with Reynolds number, correlated with the increase in vibration amplitude. At the highest Reynolds number examined, the dimensionless energy conversion ratio is 0.2, indicating that approximately 20% of the flow energy approaching the cylinder frontal cross-section can be converted to useful electrical energy. This factor increased substantially with Reynolds number from approximately 15 to 20% over the Reynolds number range considered ($Re \sim$ 1700–5900). The fit devised for the peak vibration amplitude was extended for expressing the average extracted power as a function of mass–damping and Reynolds number.

Nomenclature

c	Damping coefficient
C_A	Added mass coefficient of circular cylinder
C_v	Vortex force coefficient
C_y	Lift coefficient
D	Cylinder diameter
f_n	Natural frequency of the system in air
f_N	Natural frequency of the system in fluid
F_v	Vortex force
F_y	Lift force
G	Gap between the magnet and copper plate
k	Spring stiffness
L	Immersed length of the cylinder
m	Total mass of the cylinder-magnet assembly
m_f	Mass of the displaced fluid
m^*	Mass ratio
P	Instantaneous power
$\overline{P}$	Average power
$\overline{P}_{max}$	Maximum average power
Re	Reynolds number
U	Free stream velocity
U^*	Reduced velocity
y	Transverse displacement of the cylinder
$\dot{y}$	Transverse velocity of the cylinder
$\ddot{y}$	Transverse acceleration of the cylinder
μ_m	Magnetic dipole moment of the magnet
ν	Kinematic viscosity of the fluid
ϕ_{total}	Phase difference between lift force and displacement
ϕ_{vortex}	Phase difference between vortex force and displacement
ρ	Fluid density
ζ	Damping ratio

1. Introduction

Vortex-induced vibration may occur when a bluff body, having some degree of freedom, is placed in a fluid stream. Stationary bluff bodies experience vortex shedding above a critical Reynolds number. In this state, vortical structures form at the rear of the bluff body and are typically shed in an alternating fashion. This causes fluctuations in the lift and drag forces experienced by the body. An elastically mounted body can vibrate due to these fluctuating forces, which is known as *vortex-induced vibration* (VIV). Indeed, VIV is encountered in many important situations, for example, marine risers, bridges, transmission lines, buildings, heat exchangers, etc. Often the flexibility of the structure can be modelled as a linear spring for simplicity. Such a simplified model focuses on the resonant vibration of an elastically mounted bluff body with one or two degrees of freedom (DOF) of movement due to the oncoming fluid flow.
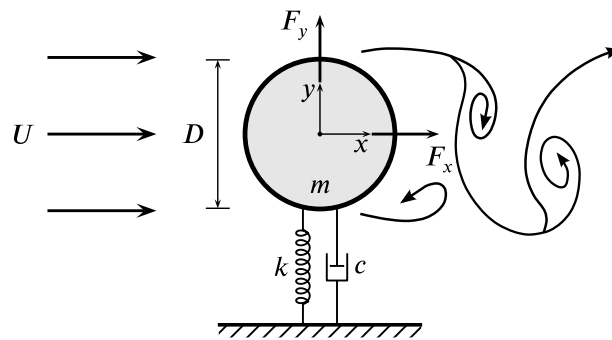
Vortex-induced vibration (VIV) of a circular cylinder has been studied extensively by many researchers; for example, see the reviews by Khalak and Williamson (1999), Williamson and Govardhan (2004), Sarpkaya (2004), Gabbai and Benaroya (2005) and Bearman (2011). The focus of many of these studies has been to identify the maximum cylinder response by minimizing the structural damping. This is important because of the possible structural failure that may occur due to large

deformations. Khalak and Williamson (1999), in their experiments with a 1-DOF elastically mounted circular cylinder, found three branches in the amplitude response: the *initial*, *upper* and *lower* branches, as the ratio of shedding frequency to body oscillation frequency was varied. The maximum vibration amplitude was close to one cylinder diameter (D) and was observed to occur in the upper branch. The transition from one branch to another was found to be associated with the changes in the vortex shedding mode and phases of the lift and vortex forces. The transition from the initial branch to the upper branch occurs when the phase of the vortex force jumps from $0°$ to $180°$, which is associated with the vortex shedding mode changing from 2S (refer to Williamson and Roshko (1988)) for a description of the different vortex shedding modes) to $2P_o$. The upper to lower branch transition is associated with a jump from $0°$ to $180°$ in the phase of the lift force and a change in the vortex-shedding pattern from $2P_o$ to $2P$. Jauvtis and Williamson (2004) conducted 2-DOF VIV experiments on a circular cylinder by using a pendulum arrangement. For mass ratios 6.0 or greater, the transverse direction response was found to be close to a 1-DOF circular cylinder. However, a super-upper branch was observed for mass ratios less than 6.0. In that state, a maximum vibration amplitude of $1.5D$ and a corresponding $2T$ vortex shedding mode were observed.

Some results on the oscillatory response have also been reported on the effect of damping. Feng (1968) used an electromagnetic-eddy-current-based damper for studies of circular and D-shaped cylinders in a wind tunnel. Due to the large mass–damping parameter (product of the mass ratio and the damping ratio), the vibration amplitude response did not have any discontinuities. Based on this, Khalak and Williamson (1999) concluded that only two branches (the initial and lower branches) are present at higher mass–damping. Klamo et al. (2005) reported the effect of Reynolds number on the maximum vibration amplitude (A^*_{max}) of a circular cylinder. They conducted experiments on VIV of circular cylinders of two different diameters for different values of mass, spring stiffness and damping values. The Reynolds number (defined by Re $= UD/\nu$, with U the free-stream velocity and ν the kinematic viscosity of the fluid) was varied in the range $525 <$ Re < 2600. Using a linear fit, they were able to extrapolate the limiting value of A_{max} at zero damping at three Reynolds numbers Re $\approx$ 525, 1000 and 2600. They concluded that along with damping, the maximum vibration amplitude depends on Reynolds number but it is independent of the mass ratio. Klamo et al. (2006) showed the transition of the VIV amplitude from the so-called *three-branch response* to the *two-branch response* with the increasing damping. They also relied on the jump in the vibration amplitude for identification of the upper branch and concluded that the three-branch response is observed at low mass–damping and high Reynolds number. They also identified the three branches in the frequency response. For low Reynolds number, they found hysteresis in the lower branch to the desynchronization region. Klamo (2009) proposed a variable magnetic eddy-current damping system to study VIV of a circular cylinder. Govardhan and Williamson (2006) controlled the damping by applying an external force to the cylinder proportional to the cylinder velocity. In their setup, the measured cylinder velocity was applied to the support of a spring connected to the cylinder to mimic the damping force. A functional fit was proposed for maximum vibration amplitude as a function of the mass–damping parameter and Reynolds number.

Studying damping effects is also important as VIV can be used for converting flow energy into electrical energy (see Bernitsas et al., 2008; Barrero-Gil et al., 2012; Soti et al., 2017). A cylinder undergoing VIV has kinetic energy and part of it can be extracted using a power transducer such as an electromagnetic generator (Soti et al., 2017). The power-extraction process from VIV introduces additional damping into the system. Therefore, the power extraction process can be modelled by adding a damper to the system. Bernitsas et al. (2008) proposed a flow energy extraction device called VIVACE which utilized VIV of circular cylinders. They showed improved energy density, a measure of the energy generated per unit volume occupied by the converter, of the VIVACE converter in comparison to three existing wave-energy converters. The average flow power conversion efficiency of the device was reported to be close to 0.22 for Reynolds number close to 9.3×10^4. The VIVACE device is submerged under the ocean surface to minimize its effects on the coastal real estate. Raghavan et al. (2009) experimentally investigate the effects of proximity to a bottom boundary on the performance of VIVACE for the Reynolds number range of 8×10^3–1.5×10^5. For large gap ratios ($G/D > 3$), VIV was found to be unaffected by the bottom boundary. For gap ratio less 3, the vibration response was partially suppressed by the bottom boundary. Lee and Bernitsas (2011) conducted an experimental study on the performance of VIVACE at various spring stiffness and damping values for the Reynolds number range of 4×10^4–1.2×10^5. The damping and stiffness of the system were mimicked by a motor and pulley system. The virtual damping and stiffness values were controlled by the torque of the external motor using software. They found an increase in the vibration amplitude with Reynolds number, and a peak vibration amplitude of $1.78D$ was achieved for a smooth cylinder for the lowest damping. The maximum harnessed power was close to $0.33 \times \frac{1}{2}\rho DLU^3$ for Reynolds numbers close to 7.5×10^4.

All of the previous studies relied on the jumps in the amplitude response for identification of the three branches of VIV response. However, the jumps in the vibration response disappear at higher damping. It will be shown that frequency can be used to demarcate the three branches at higher mass–damping. The main focus of the previous studies on damped VIV of circular cylinders has been on the effect of damping on the peak amplitude response. This is summarized in a "Griffin plot", which plots peak vibration amplitude as a function of mass–damping. Literature studied showed considerable scatter about the underlying functional variation. Klamo et al. (2005) and Govardhan and Williamson (2006) have shown that the scatter is mostly due to the Reynolds number differences between different measurements. In the present work, an accurate physical damping mechanism is used to confirm that the data points on the Griffin plot show virtually no scatter for a fixed Reynolds number. By conducting experiments for three different Reynolds numbers, it is confirmed that the scatter is due to Reynolds number differences. The functional dependence of the undamped peak vibration amplitude on Reynolds number, predicted by Govardhan and Williamson (2006), is confirmed by our measurements. Govardhan and Williamson (2006) also proposed a quadratic fit for the peak vibration amplitude as a function of mass–damping which did not behave physically (predicted

Fig. 1. Definition sketch for the transverse vortex-induced vibration of a circular cylinder. The hydro-elastic system is idealized as a 1-DOF system constrained to move in the cross-flow direction. Here, U is the free-stream velocity, k the spring constant, D the cylinder diameter, m the oscillating mass, and c the structural damping. F_x and F_y represent the drag and the transverse lift force components acting on the body, respectively.

increasing amplitude with increasing damping) at high mass–damping. A modified fit is proposed which is well behaved while maintaining the level accuracy. Apart from the Griffin plot, which focuses only on peak amplitude response, the effects of damping on the amplitude response as a function of reduced velocity appears to have been insufficiently documented in the literature, which may be important for engineering applications that may not always operate at the optimal operating point. The aim of the present work is also to report the effects of damping on various parameters of the VIV response of the circular cylinder, namely, the amplitude, frequency, lift and phase. As it is clear from the literature review, there is a lack of data on power extraction for low ranges of Reynolds number ($1000 < \text{Re} < 10{,}000$). To fill this gap, the power extracted by the damping system from VIV of the circular cylinder is investigated for this range of Reynolds number.

2. Experimental methodology

2.1. Experimental apparatus

The experiments reported on here were conducted in the free-surface recirculating water channel of the *Fluids Laboratory for Aeronautical and Industrial Research* (FLAIR) group at Monash University. The water channel has a test section with dimensions of 600 mm in width, 800 mm in depth and 4000 mm in length. Fig. 1 shows a schematic of transverse VIV of a circular cylinder, which defines key parameters to the problem. The elastically mounted cylinder is free to oscillate in only one direction transverse to the oncoming free-stream. The governing equation of the oscillating system can be expressed as

$$m\ddot{y} + c\dot{y} + ky = F_y, \tag{1}$$

where m is the total oscillating mass of the system, c is the structural damping, k is the structural stiffness, y is the body displacement in the transverse (cross-flow) direction and F_y is the transverse lift force.

In the present experiments, the hydro-elastic VIV set up employed a low-friction air-bearing system. A schematic of the experimental set up is shown in Fig. 2. The air bearing consisted of two air bushings that moved along two stationary precision guiding shafts. The air bushings were mounted on a carriage to which the cylinder was attached (see Sareen et al., 2018). The test circular cylinder, precision-made from hollow aluminium tubing, had a diameter of $D = 30 \pm 0.01$ mm. The immersed length in water was $L = 615$ mm, giving the mass of displaced fluid of $m_f = \rho\pi D^2 L/4 = 434$ g and a length-to-diameter aspect ratio of 20.5. The total oscillating mass was $m = 1301.5$ g, yielding an overall mass ratio of $m^* = m/m_f = 3.0$. A non-contact digital optical encoder with a resolution of 1 μm (model: RGH24, Renishaw, UK) was mounted to the side of the carriage to measure the displacement of the cylinder. An end-conditioning platform was used to reduce end effects at the bottom edge of the cylinder as shown in the schematic (see Zhao et al., 2014a, b; Wong et al., 2017). A force balance based on strain gauges was mounted between the carriage and the cylinder for directly measuring the fluid forces. However, it should be noted the transverse lift was derived based on the body displacement signal and other system parameters in Eq. (1), since it was found that the accurate digital displacement signal produced a more reliable and accurate lift force than attainable from the force balance signal because of electrical noise. The method and approach have been further described and validated in Zhao et al. (2014b) and Wong et al. (2017).

The data acquisition (DAQ) system consisted of a USB DAQ device (model: USB6218-BNC, National Instruments, US) and customized LabVIEW programs that controlled the water-channel flow velocity and automation of measurements. For each U^* case, the DAQ measurements were sampled at 100 Hz for more than 100 oscillation cycles. Spot measurements with longer sampling times verified that this signal acquisition time was sufficient to provide reliable and accurate response amplitudes.
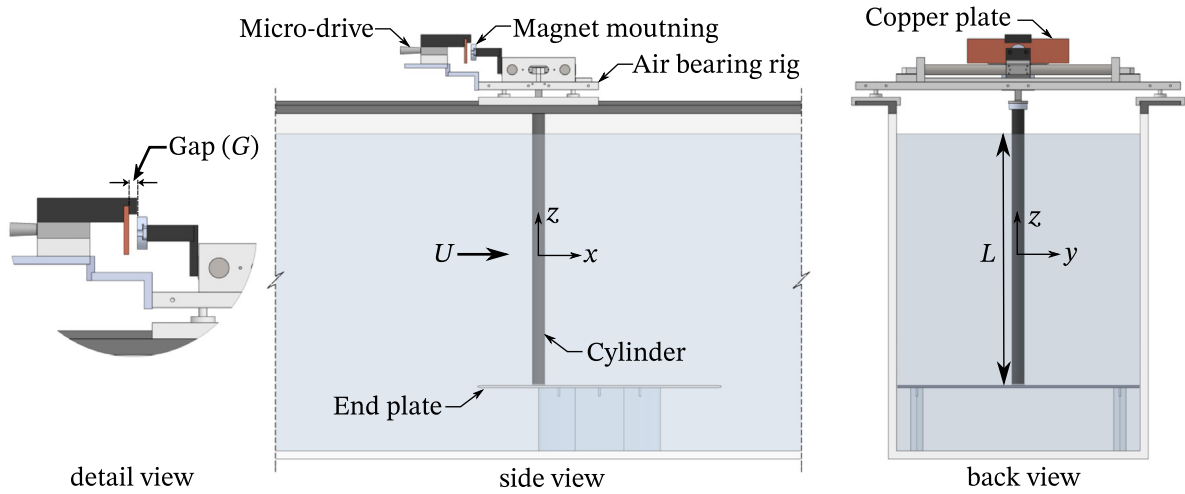
Fig. 2. Schematic of the experimental set-up used for the VIV experiments.

2.2. Damper mechanism

An eddy-current based damping mechanism was used to achieve controlled and variable damping values. The damper consists of a stationary electrically conductive plate and a permanent magnet that can move along the length of the plate at any fixed gap (G) between the plate and the magnet. When the magnet moves relative to the plate it creates eddy currents inside the plate. These eddy currents produce their own magnetic field that opposes the motion of the magnet (Lenz's law). From an energy conversion point of view, the eddy currents dissipate energy in the form of heat due to the electrical resistance of the plate. The dissipated energy is deduced from the kinetic energy of the magnet. If the magnet is located at a distance G from the plate and moves with a constant velocity $\dot{y}$ along the y-direction (see Fig. 3) then the damping force can be expressed as (Schieber, 1975; Klamo, 2009)

$$F = C\sigma\delta B_x^2\dot{y}, \tag{2}$$

where σ and δ represent the electrical conductivity and thickness of the plate, respectively. The constant C is a function of various parameters such as the dimensions of the plate and the magnet. It also accounts for the variation in magnetic field along the plate and the finite width of the plate. The magnetic field strength B_x depends on the gap G, material and size of the magnet. The strength of magnetic field at any point P on the plate is given by (Donoso et al., 2009)

$$B_x = \frac{\mu_m}{(G^2 + r^2)^{3/2}}\left[\frac{3G^2}{G^2 + r^2} - 1\right], \tag{3}$$

where μ_m represents the magnetic dipole moment of the magnet. Eqs. (2) and (3) show that the damping coefficient ($c = C\sigma\delta B_x^2$) depends upon various parameters, namely: the gap between the magnet and the plate, the magnetic field strength of the magnet, and the size, thickness and material of the conducting metal plate. A change in the damping, in the present experiments, is achieved by changing the gap between the plate and the magnet.

The damper system that was made for the current experiments is shown in Fig. 4. For the present experiments, an N42 grade rare earth Neodymium magnet element of cylindrical shape with diameter 20 mm and length 10 mm was used. The magnet element was mounted on the carriage to which the cylinder is attached so that it followed the motion of the cylinder. A copper plate of 250 mm length and 60 mm width was used. It had a thickness of 6 mm. This plate was attached to a micro-drive stage so that the distance between the magnet and plate can be changed in a precise and controlled manner with an accuracy of 10 μm. This allowed the magnet element to remain at the same gap irrespective of its transverse location so that the damping ratio could be set to a constant at any given gap. This was achieved by mounting the linear stage on an orientation plate having some degree of freedom to rotate about the vertical axis. The orientation plate was locked in a position where the line of movement of the magnet was parallel to the plate. This ensured that the damping coefficient did not vary with the transverse location of the body. The orientation plate was mounted on a extension plate which had series of holes to attach the extension plate at the desired gap.

2.3. Damping measurements

The first experimental step was to measure the damping coefficient for various gap values so that any desired damping value, c, can be achieved by positioning the copper plate at the corresponding gap distance, G, from the magnet element. The
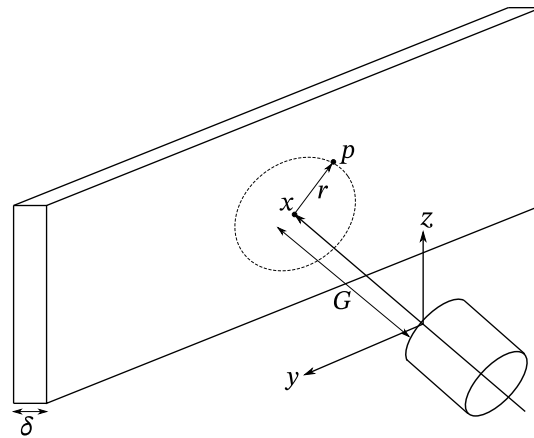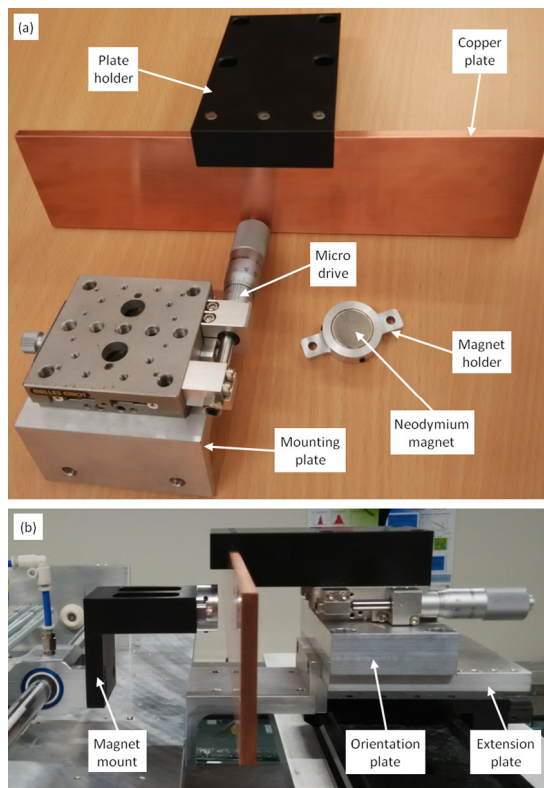
Fig. 3. Schematic of the damper system.

Fig. 4. (a) Various components of the damper system and (b) the damper assembly attached to the VIV setup.

damping coefficient was measured by conducting free-decay tests in air. The cylinder was removed during the free decay test to avoid fluid forces and an equivalent mass was placed on the carriage to retain the total mass of the system. If the system is displaced by some distance A_0 from its equilibrium position and released then the motion of the freely vibrating system is governed by

$$m\ddot{y} + c\dot{y} + ky = 0, \tag{4}$$

where m and k represents the total mass and stiffness of the system. The behaviour of the solution of Eq. (4) depends upon the damping ratio $\zeta = c/(2m\omega_n)$ where $\omega_n = \sqrt{k/m}$ is the angular natural frequency of the system. For damping ratios, $0 \leq \zeta < 1$, the system undergoes periodic harmonic motion of form $y = A\cos(\omega_d t)$, where $\omega_d = \omega_n\sqrt{1-\zeta^2}$ is the
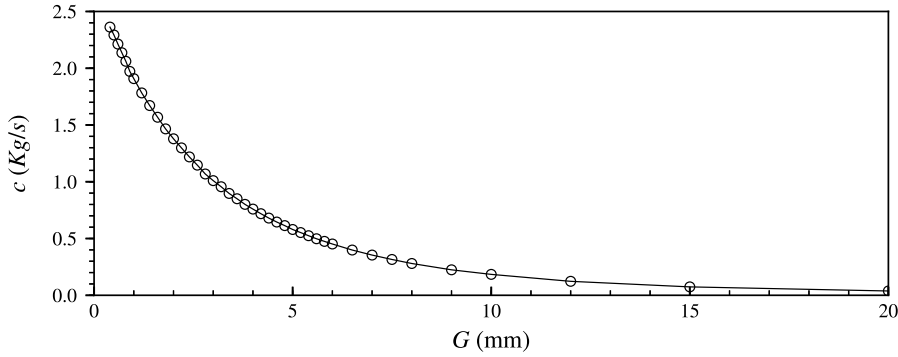
Fig. 5. Damping coefficient (c) as a function of the gap (G) between the magnet and the copper plate of the damper used in the present experiments.

damped natural angular frequency and the amplitude of vibration is given by $A = A_0 \exp(-\zeta \omega_n t)$. Two consecutive peaks of displacement would be separated by the time interval $T = 2\pi / \omega_d$. If the log decrement between two instances of peak displacement, t_n and $t_{n+1} = t_n + T$, is defined as $\delta = \ln(A_n/A_{n+1})$ then the damping ratio is given as

$$\zeta = \sqrt{\frac{\delta^2}{4\pi^2 + \delta^2}}. \tag{5}$$

The natural frequency can be calculated as $f_n = 1/T$ for very low ζ cases. At any gap, the damping values obtained by applying Eq. (5) to all the consecutive peaks of the displacement are averaged to give a mean damping at that gap. Since the damping coefficient is independent of mass and stiffness of the system, it is useful to convert the damping ratio values to a damping coefficient. The measured values of the damping coefficient as a function of the gap (G) are plotted in Fig. 5 for $m = 1301.5$ g and $f_n = 1.095$ Hz.

2.4. Experimental validation

The experimental set-up was validated by comparing the amplitude response of the circular cylinder at low damping with that of Khalak and Williamson (1997) and Zhao et al. (2014a). The mass and damping ratios for the present case are $m^* = 3.0$ and $\zeta = 2.5 \times 10^{-3}$. Fig. 6 shows a good match of the amplitude response of the cylinder with previous results. The difference in the peak value of the amplitude could be attributed to the difference in the Reynolds number. The Reynolds number range for the data presented in Fig. 6 is given by the dataset 3 in Table 1. The synchronization region, i.e. the range of reduced velocity for which the cylinder shows significant vibration amplitude, is known to shrink with the increase in the mass ratio. Since the mass ratio for the present experiments is slightly higher than that of Khalak and Williamson (1997), the boundaries of the upper and lower branches do not match exactly with the published data. Overall, a good match is obtained and the three response branches, the initial, upper and lower branches, are captured.

3. Results

In this section, the effects of damping on the vortex-induced vibration of a circular cylinder will be discussed. There are four important independent parameters in the study of VIV: the mass ratio (m^*), damping ratio (ζ), reduced velocity (U^*) and Reynolds number (Re). The reduced velocity is defined as $U^* = U/(f_N D)$, where U is the free stream velocity and f_N is the natural frequency of the system in water. The natural frequency in water is measured by conducting free decay tests in still water with minimal damping (without the damper). The VIV response also depends on the Reynolds number (see Klamo et al., 2005). In the present experiments, the reduced velocity was varied by changing the free-stream velocity while keeping the values of f_N and D fixed. This also resulted in a changing Reynolds number. Three sets of f_N values were used in the experiments to examine the effect of Reynolds number. The values of natural frequency and corresponding Reynolds number ranges for the three sets are shown in Table 1. The mass ratio is kept at $m^* = 3.0$. The change in f_N was achieved by physically changing the number of springs and thereby changing the spring constant. The displacement and force data were recorded for 360 s (for more than 100 oscillation cycles) for a single reduced velocity.

3.1. Effect of damping on the vibration response

The effect of damping on the vibration amplitude of the circular cylinder is shown in Fig. 7 for the Reynolds number range of Re = 2220–6661 (referred to as set 2 in Table 1). For the least damped case, a typical three-branch VIV response is observed. In the initial branch, $3.6 \leq U^* < 4.8$, the vibration response is influenced by the vortex shedding frequency
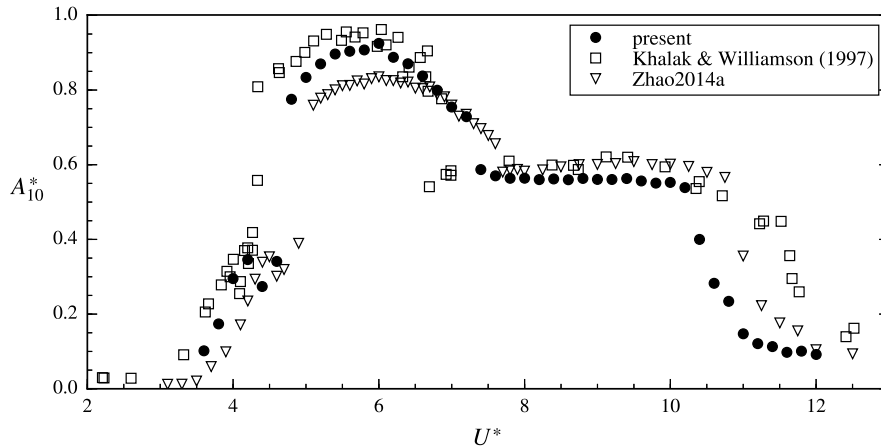
Fig. 6. Comparison of displacement amplitude obtained by our experiment ($m^* = 3.0$, $\zeta = 2.5 \times 10^{-3}$ and $3805 <$ Re < 11416) with that of Khalak and Williamson (1997) ($m^* = 2.4$, $\zeta = 4.5 \times 10^{-3}$ and Re ≈ 6000 in the lower branch) and Zhao et al. (2014a) ($m^* = 2.66$, $\zeta = 3.2 \times 10^{-3}$ and $1450 <$ Re < 7500).

Table 1
Three set of experiments performed in the present work.

| Set	Natural frequency in air f_n (Hz)	Natural frequency in water f_N (Hz)	Re range
1	0.362	0.309	1250–3750
2	0.639	0.550	2220–6661
3	1.095	0.943	3805–11416

for a stationary cylinder and the natural frequency of the system in the fluid, which is based on the effective added mass that varies with the reduced velocity. The initial branch is further divided into a quasi-periodic (QP) region (see Fig. 8(a)) for $3.6 \leq U^* < 4.4$, and a periodic (P) region for $4.4 < U^* < 4.8$ (Fig. 8(b)). There is a visible jump in the vibration amplitude from the initial to the upper branch at $U^* \simeq 4.8$. At the start of the upper branch, which extends over $4.8 \leq U^* \leq 7.4$, the vortex shedding frequency locks onto the natural frequency of the cylinder and the amplitude response becomes significantly higher. The amplitude response reaches its peak value of $A_{10}^* \approx 0.8$ at $U^* = 5.8$ in the upper branch. Here, A_{10}^* represents the mean of the top 10% of peaks of the displacement signal. The vibration amplitudes were observed to be varying from one cycle to another, i.e. the vibrations are not fully periodic (see Fig. 8(c)). With further increase in U^*, the vibration response switches to the lower branch covering $7.4 \leq U^* \leq 11.0$. The vibration amplitude response does not vary much with U^* in the lower branch and is consistently close to $A_{10}^* \approx 0.6$ (see Fig. 8(d)). The vibration amplitude is also quite stable from one cycle to another at any U^* i.e. the vibrations are periodic. The upper and lower branch combined is called the lock-in region. The cylinder motion desynchronizes from the vortex shedding frequency for $U^* > 11.0$ and the vibration amplitude jumps down to a small value.

The vibration amplitude is seen to decrease with an increase in the damping ratio for any reduced velocity since the role of damping is to dissipate energy. The jump in the vibration amplitude at the initial to upper branch transition becomes smeared out with increasing damping and the beginning of the upper branch gets delayed. On the other hand, the reduced velocity corresponding to the end of the lower branch decreases with the damping. As seen in Fig. 7, these critical reduced velocities lie approximately on a straight line. Therefore, the lock-in region becomes narrower as the damping ratio is increased. The transition between the branches become continuous rather than through jumps. The vibration amplitude in the lower branch tends to decrease with U^* at higher damping values. The upper and lower branches are identified by blue and red colours, respectively, in Fig. 7. The identification of boundaries of these branches, especially the upper branch, is approximate at high damping values and the proposed classification will be discussed in the next section. Klamo et al. (2006) had also plotted the variation of the vibration amplitude of the cylinder with the reduced velocity for various damping values to show the transition from the three-branch response to the two-branch response. The mass ratio in their experiments (=49.8) was much larger than that of the present case. In their experiments, Reynolds number at the maximum vibration amplitude was close to 1000, while for the present work it is close to 3200. Despite these differences in the operating parameters, they also found a delay in the jump from initial to upper branch and smaller synchronization regions with increasing damping. In addition, they found that the upper to lower branch transition point did not change with the damping. Fig. 7 shows that this is true only up to a certain damping value (for $\zeta \leq 0.074$ in the present work) after which this transition occurs at a lower U^* as the damping is increased. Govardhan and Williamson (2006) also plotted the vibration amplitude as a function of reduced velocity and damping for $m^* = 10.0$ and Re ≈ 4000. By comparing the vibration responses from the two studies with the present work, it can be concluded that the magnitudes of the jump in the vibration amplitude (for initial to upper
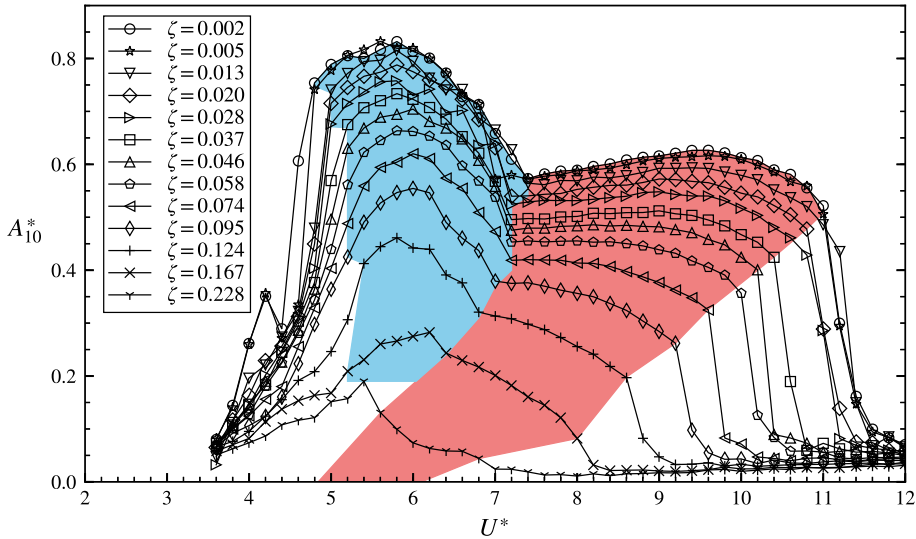
Fig. 7. Mean of top 10% maximum amplitude response (A_{10}^*) versus reduced velocity for various values of damping ratios. The mass ratio is 3.0 and Reynolds number ranges from 2220 to 6661 as reduced velocity is increased. Blue and red regions show the upper and lower branches, respectively. (For interpretation of the references to colour in this figure legend, the reader is referred to the web version of this article.)
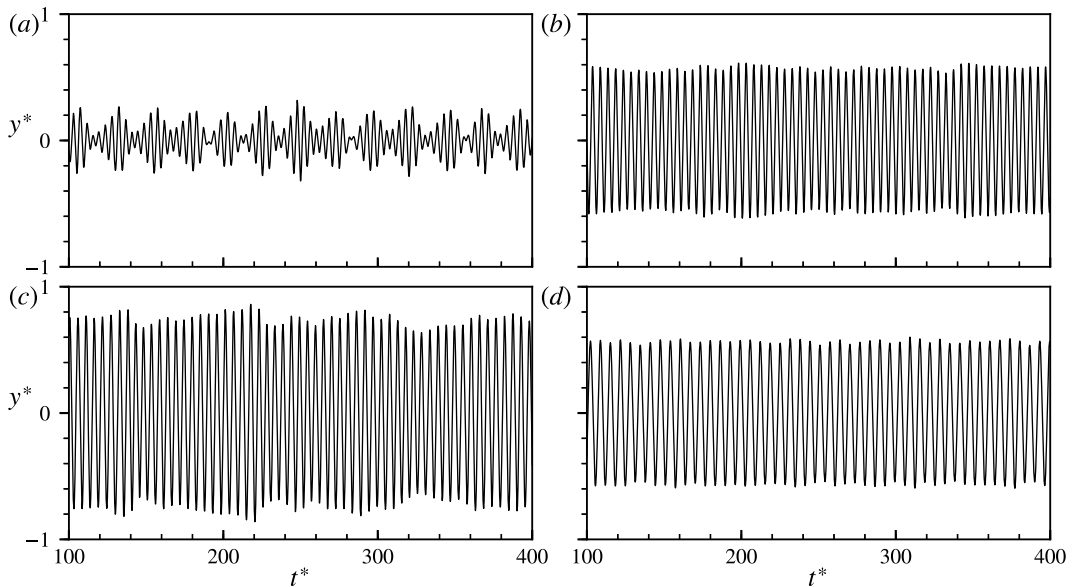
Fig. 8. Time histories of the non-dimensional cylinder displacement for U^* = (a) 4.0, (b) 4.6, (c) 5.8 and (d) 8.0 for the minimal damping case. The plots illustrates the time-variation of the cylinder displacement for quasi-periodic, periodic, upper branch and lower branch regions, respectively.

branch and upper to lower branch transitions) and the peak vibration amplitude are a decreasing function of mass–damping and an increasing function of Reynolds number.

Both of the previous studies relied on the jump in the vibration amplitude at the end of the initial branch to identify the onset of the upper branch. This approach raises a question: which values of change in the vibration amplitude, for a given small change in the reduced velocity, can be considered as a jump? No information is available on this in the literature. Furthermore, both the studies have concluded that there is no upper branch at low Reynolds number (Re $\leq$ 525) even at zero damping since the vibration amplitude is a continuous function of the reduced velocity for these cases. In fact, Govardhan and Williamson (2006) labelled $A^* = 0.6D$ as the boundary between the three-branch and two-branch response regions since it is the peak vibration amplitude at low Re. In contrast, Leontini et al. (2006), by performing numerical simulations at Re = 200, have shown that the low Re vibration response of the cylinder shows regions similar to the upper and lower branches found in the high Re experiments. Therefore, vibration amplitude does not seem to be a definitive indicator of the

branching behaviour of VIV at low Re and high damping. In the following section, frequency response will be shown to be alternative candidate for identification of different branches in the damped VIV response of low mass-ratio circular cylinder.

Blevins and Coughran (2009) plotted the vibration response of a circular cylinder at six damping values for $m^* = 6.4$ and Re $\approx$ 30 000 at peak vibration amplitude. For the lowest damping case, the lower branch region in their work shows a monotonic decay of the amplitude with the reduced velocity. In contrast, the vibration amplitude in our results stays around $0.6D$ in the lower branch which is consistent with the results of Govardhan and Williamson (2006) and Khalak and Williamson (1997). A similar monotonic decay of the vibration amplitude in the lower branch can be seen in the result of Lee and Bernitsas (2011) where Reynolds number was close to 90,000 at the peak vibration amplitude. Therefore, this different nature of the lower branch could be a Reynolds number effect. Both Blevins and Coughran (2009) and Lee and Bernitsas (2011) did not focus on the three-branch to two-branch response transition as the damping was increased.

3.2. Effect of damping on the oscillation frequency

The normalized frequency ratio of vibration frequency to the natural frequency of the cylinder in water ($f_y = f/f_N$) also shows different behaviour in the three response branches. A contour plot of amplitude spectral density (ASD) of cylinder displacement against normalized frequency and reduced velocity is plotted on the left of Fig. 9 for five different damping values. A contour map of the ASDs of the lift force signals is also plotted on the right of Fig. 9. The log scale is chosen for the ASD in the contour plots so that weak harmonics can still be recognized. For low damping values (see Fig. 9(a)), three distinct patterns are seen for the frequency response. In the initial branch, two frequency components are present in the displacement. One is due to the vortex shedding frequency, which overlaps with the straight line representing $St = 0.208$ in Fig. 9, and the other is due to the natural frequency of the system. The two components are also visible in the lift force, as seen in Fig. 9(a). The vortex shedding frequency becomes locked to the natural frequency of the cylinder at the start of the upper branch and there is only one dominant component present in f_y. The normalized vibration frequency of the cylinder jumps to a value close to unity at the start of the upper branch. The normalized vibration frequency then increases gradually, with a slope slightly less than the St slope, with U^* through the upper branch. A third harmonic of the fundamental frequency appears in the lift signal in the upper branch, which could be related to the change in vortex shedding pattern from $2S$ to $2P_o$ (Morse and Williamson, 2009). With a further increase in U^*, another jump in f_y is observed at the start of the lower branch. The normalized vibration frequency stays constant at a value greater than 1.0 ($\approx$ 1.25) in the lower branch. The vibration amplitude in this branch is very stable compared to the initial and upper branches and therefore, the plots show a sharp spectral peak through this lower branch. However, a relatively stronger third harmonic is present in the lift force in the lower branch indicating that the signal is not purely sinusoidal. For $U^* > 11.0$, the desynchronization region appears and the cylinder displacement shows two dominant frequencies: the vortex shedding and the natural frequencies. The lift force also has these two frequency components in this region. Note that in the contour plots the energy of the signal is distributed over a range of frequencies.

As the damping is increased, the desynchronization region begins at progressively small values of U^*. All contour plots in Fig. 9(b)–(e) show a region similar to Fig. 9(a), where the normalized vibration and lift frequencies remain at a constant value. Following the discussion for the low damping case in the previous paragraph, this region can also be labelled as the lower branch for higher damping cases. The right-hand end of the lower branch can be identified by the distribution of the displacement and lift signal energy to a larger range of frequencies i.e. the scatter in the ASD frequency content. The left-hand end of the lower branch occurs when the normalized vibration frequency stops changing with U^* and becomes a constant. The same can be seen for the third harmonic in the lift force. There is a region in Figs. 9(b) to 9(e) resembling the initial branch for the low damping case in Fig. 9(a) where the vibration frequency matches the vortex shedding frequency for a stationary circular cylinder. The frequency content overlaps with the $St = 0.208$ line in this region. Due to the similarity, it is reasonable to designate this region the initial branch for higher damping cases.

Identifying the start of the upper branch is less obvious at higher damping values. In Fig. 9(b), which corresponds to an order of magnitude higher damping, the start of the upper branch can still be identified by a jump in the vibration frequency. A small jump in the vibration frequency is also present at the boundary of upper and lower branches since there is a visible change in the amplitude variation with U^* across the branch boundaries (see Fig. 7). In Fig. 9(c), f_y does not show any visible jump at the upper branch boundary since the vibration amplitude increase gradually with U^* at this high damping. The vibration frequency still shows the three different trends that occur in the three branches at low damping. In the upper branch of the low damping case, the normalized vibration frequency increases with U^* but no longer overlaps with the $St = 0.208$ line, and a third harmonic of the fundamental frequency appears in the lift force. These two trends are also present for the higher damping cases and, therefore, were used for identifying the upper branch at high damping. Notice that in Fig. 9(e), there is a very narrow region of U^* for the upper branch where the normalized vibration frequency deviates from $St = 0.208$ line and a third harmonic is present in the lift force. Therefore, this can act as a demarcation boundary between the three-branch and two-branch types of VIV responses. The corresponding vibration amplitude is close to $0.2D$ which is three times smaller than $0.6D$ limit set by Govardhan and Williamson (2006). Beyond this damping value, the vibration response can be considered to have only the initial and lower branches.

Govardhan and Williamson (2000) presented two normalized vibration frequency responses for a low and a high mass–damping case by changing the mass ratio. Unlike the present work, the normalized vibration frequency in the upper branch did not vary with the reduced velocity at the low mass–damping and remained close to unity for the entire synchronization
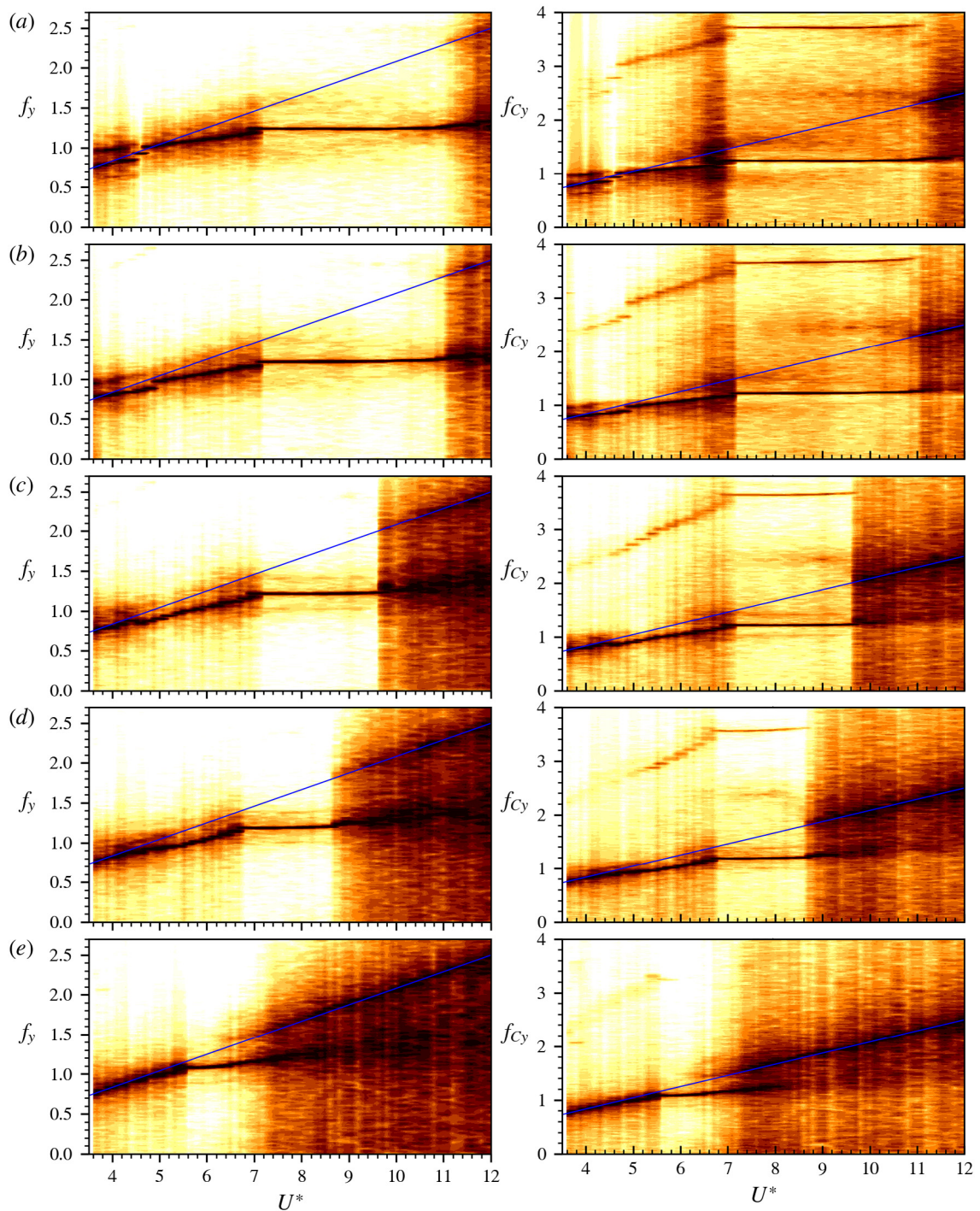
Fig. 9. Contours of the amplitude spectral density of displacement (left) and lift force (right) plotted against the normalized frequency and reduced velocity for ζ = (a) 0.002, (b) 0.028, (c) 0.074, (d) 0.124 and (e) 0.228. Each power spectrum is plotted vertically and stacked together horizontally from each U^* to form these contour plots. A $\log_{10}$ scale is used to highlight the variation from 0 (black) to -3 (white). The line represent $St = 0.208$, corresponding to the vortex shedding frequency of a stationary cylinder.

region at the higher mass–damping. These differences are most likely due to the higher value of the mass ratios in their experiments, which results in negligible effects of the effective added mass. Note that the frequency response will depend on the mass ratio since the added mass will affect the natural frequency of the cylinder in the fluid. Therefore, it was essential
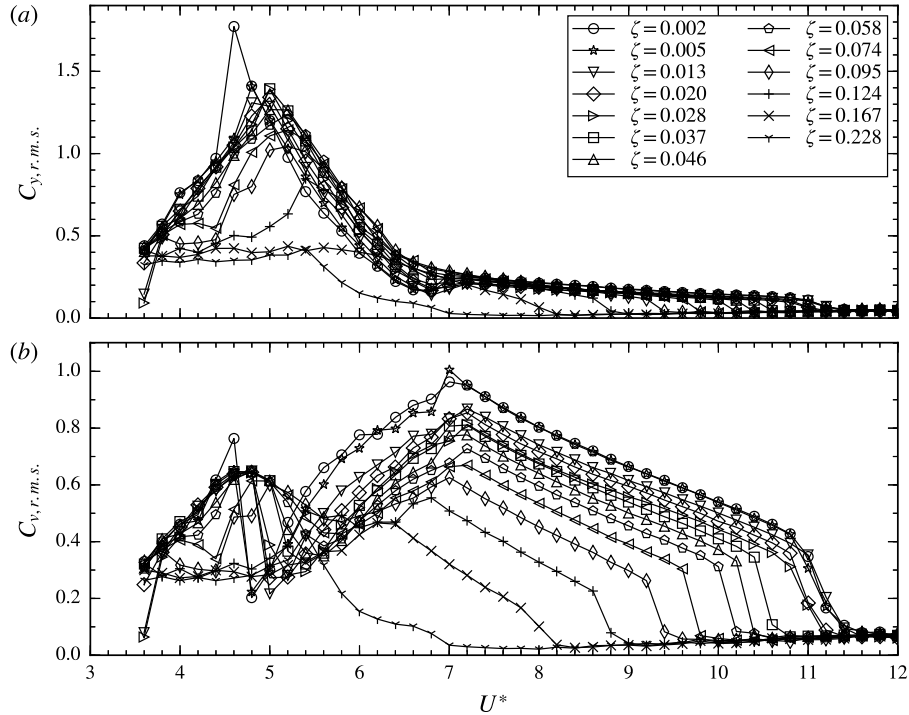
Fig. 10. (a) RMS lift coefficients, and (b) RMS vortex force coefficients versus reduced velocity for specified damping ratios.

to keep the mass ratio fixed at a low value and change the damping to see the effects of increased mass–damping on the frequency response of VIV.

3.3. Effect of damping on lift force and phase

The lift coefficient is defined by $C_y = F_y/(\frac{1}{2}\rho U^2 DL)$, where F_y represents the force acting on the cylinder in the transverse direction. The root mean square (RMS) lift coefficient as a function of reduced velocity is plotted in Fig. 10(a) for various damping ratios. The peak value of C_y is seen to decrease with an increase in damping. The maximum value of the lift coefficient ($= 1.8$) is obtained at minimum damping for $U^* = 4.6$. For small damping values, the lift force shows a rapid increase with U^* in the initial branch and reaches a peak value at the beginning of the upper branch. In the upper branch, the lift force experiences a rapid decrease with U^* and reaches a value lower than that of the stationary cylinder case. With a further increase in U^*, the lift force shows a slow decrease in its value in the lower branch. At the end of the lower branch, a jump is seen in C_y and it reduces to an even smaller value.

The fluid force can be decomposed into two components: the potential force (F_{pot}) and the vortex force (F_v). This decomposition reflects the fact that any velocity field can be constructed from the summation of a potential flow component plus a field due to the vorticity in the system. The potential force is the part of the fluid force that is in phase with the displacement (in the equivalent potential flow system). Physically, it is the force required to accelerate the surrounding fluid. Therefore, the magnitude of potential force is equal to the added mass times the acceleration of the cylinder

$$F_{pot} = -m_A \ddot{y} = -C_A \frac{\pi}{4} \rho D^2 L \ddot{y}, \tag{6}$$

where m_A and C_A ($= 1.0$ for the circular cylinder) are the added mass and potential added mass coefficient, respectively. The vortex force is then calculated by subtracting the potential force from the total lift force. The RMS vortex force coefficient ($C_v = F_v/(\frac{1}{2}\rho U^2 DL)$) is plotted in Fig. 10(b) against U^* for various damping values. The vortex force increases with U^* in the initial branch and reaches its peak at the start of the upper branch. There is a sudden decrease in C_v at the start of the upper branch. The vortex force increases with further increase in U^*. In the lower branch, the vortex force is seen to decay almost linearly with U^*.

It is also important to examine the phase of the fluid forces with respect to the displacement. The phase difference was calculated by performing a Hilbert transform of the displacement and force signals, e.g., see Khalak and Williamson (1999). Fig. 11(a) and 11(c) shows the instantaneous phase of the lift force for $U^* = 4.6$ and 6.6, respectively, for the minimal damping case. As seen in Fig. 11(a), the lift force is in phase with the displacement in the initial branch since the phase difference
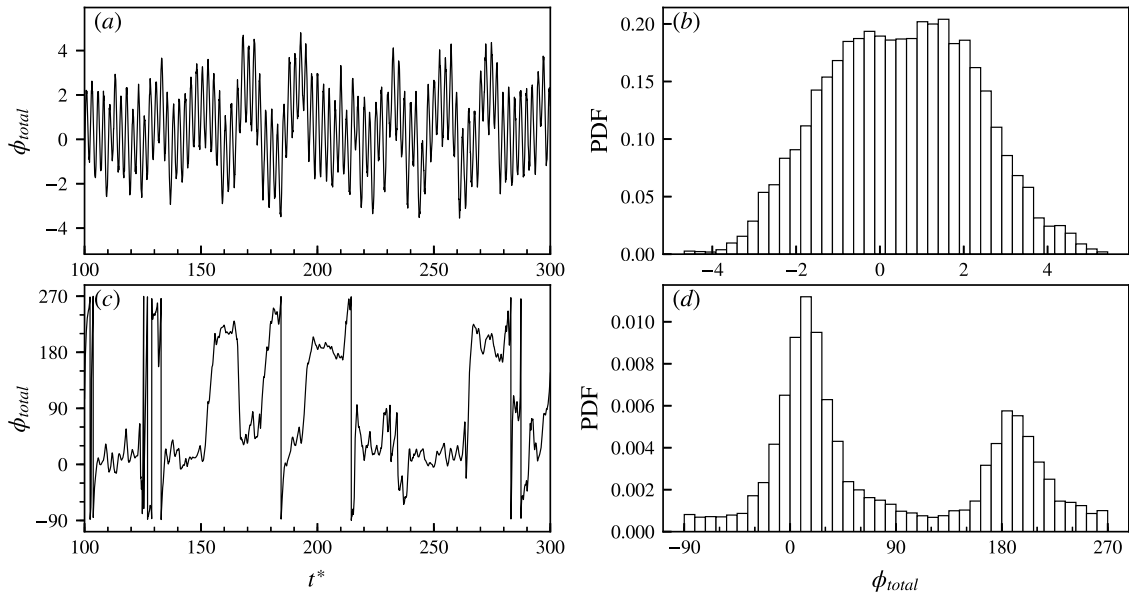
Fig. 11. Instantaneous phase of the total lift (left) and its histogram normalized to show the probability density function (right) for $U^* = 4.6$ (top) and 6.6 (bottom). All the plots corresponds to the minimal damping case.
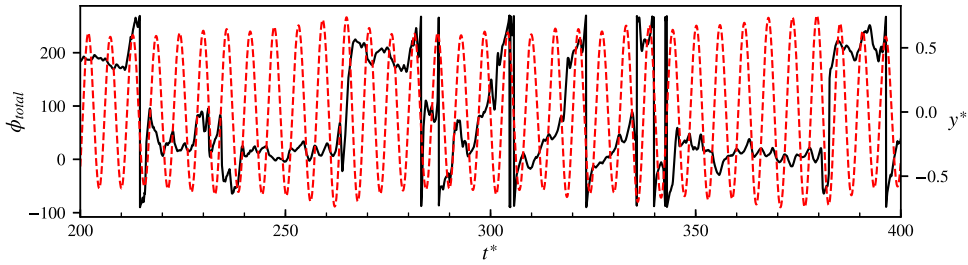
Fig. 12. Instantaneous phase of the total lift (black solid lines) and cylinder displacement (red broken lines) at $U^* = 6.6$ for the minimal damping case. This figure illustrates that the jump in phase angle is associated with the change in the nature of variation of the vibration amplitude with time.

remains close to 0°. This is evident in the histogram shown in Fig. 11(b), normalized to show the probability density function (PDF), which looks like a Gaussian distribution with zero mean value. In the upper branch, Fig. 11(b), the instantaneous phase difference jumps between 0° and 180° as evident in Fig. 11(d). Fig. 12 shows the instantaneous phase for $U^* = 6.6$ along with the cylinder displacement. It can be seen that the variation in the vibration amplitude is associated with the jumps in the phase of the lift force. The vibration amplitude is increasing or decreasing with time depending on whether the phase is close to 0° or 180°, respectively. The mean phase difference between lift force and cylinder displacement (ϕ_{total}) is shown in Fig. 13(a) for various damping ratios. The mean phase of vortex force with respect to displacement (ϕ_{vortex}) is shown in Fig. 13(b). For very low damping values, the total phase remains at 0° during the initial and upper branch. The total phase jumps to 180° during the transition from the upper branch to lower branch. The vortex phase, on the other hand, shows a jump from 0° to 180° at the start of the upper branch. These jumps in the total and vortex phase agree with those observed by Govardhan and Williamson (2000) and Khalak and Williamson (1999). The jump in the vortex phase is associated with the change in the wake structure from 2S to 2P mode. As the damping ratio is increased, the phase changes between the branches become more continuous. In addition, the phase difference between branches tends to reduce with increasing damping.

3.4. The griffin plot

Previous studies have attempted to relate the peak vibration amplitude of a circular cylinder undergoing VIV with the product of mass and damping ratios ($m^*\zeta$). Griffin (1980) plotted the peak vibration amplitude against the Skop-Griffin parameter $S_G = 2\pi^3 S^2 (m^*\zeta)$, where S is the Strouhal number for a stationary cylinder. This is known as the *Griffin plot*. Govardhan and Williamson (2006) proposed, what they called, the *modified Griffin plot*, where they plotted the peak vibration amplitude against the logarithm of mass–damping parameter $\alpha = (m^* + C_A)\zeta$. For Reynolds numbers in range of 500 to 33 000, they found a fit for the peak vibration amplitude of circular cylinder at zero damping with Re as
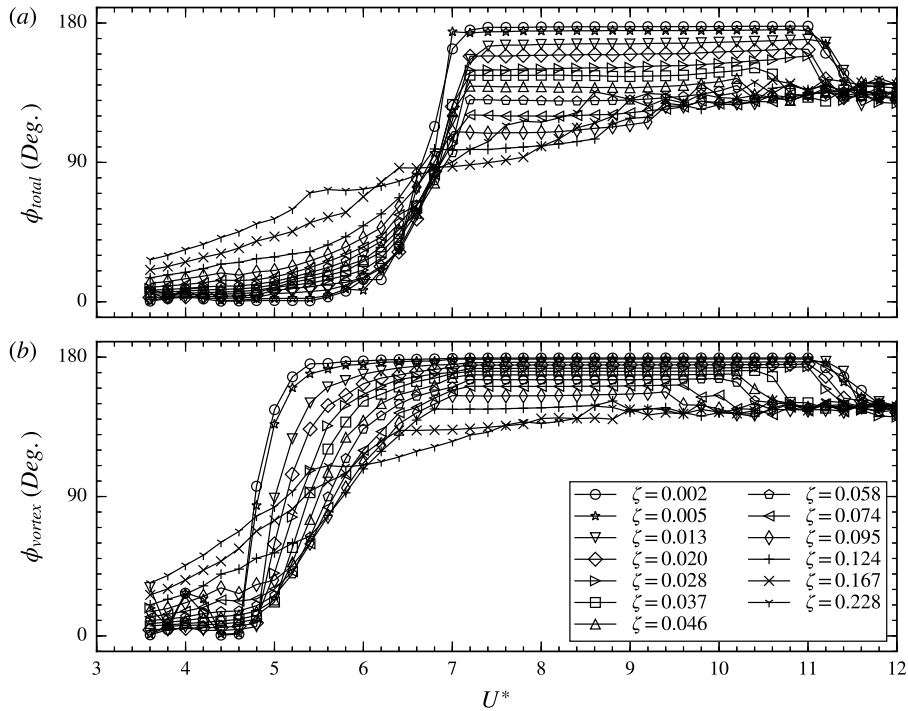
Fig. 13. Mean phase difference between (a) total lift and (b) vortex force and displacement versus reduced velocity for various values of damping ratios.
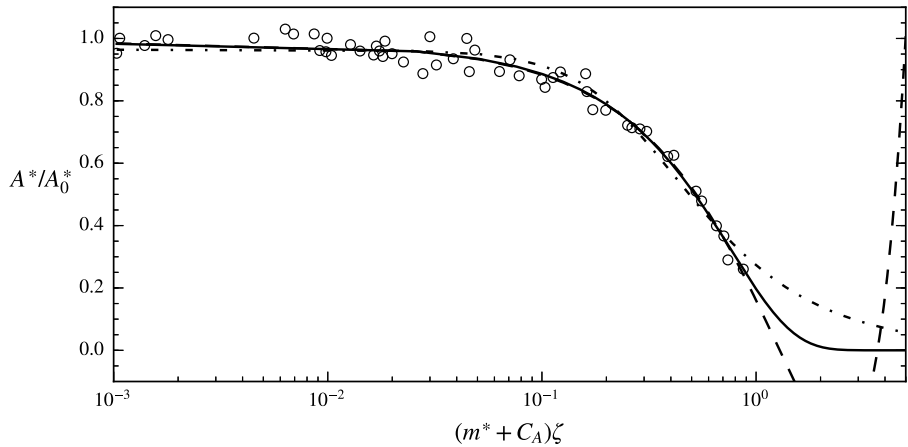

Fig. 14. Comparison of the quadratic polynomial fit by Govardhan and Williamson (2006) (dashed line), fit proposed by Sarpkaya (1978) (dash–dot line) and Eq. (7) with $n = 2$ (solid line).
Source: The data points shown as circular symbols are taken from Govardhan and Williamson (2006).

$A_0^* = \log_{10}(0.41\mathrm{Re}^{0.36})$. At a fixed Re, they proposed a quadratic polynomial fit between the peak vibration amplitude and mass–damping parameter. Overall, the peak vibration amplitude as a function of mass–damping and Reynolds number is written as $A^* = (1 + C_1\alpha + C_2\alpha^2)\log_{10}(0.41\mathrm{Re}^{0.36})$ where C_1 and C_2 are constants.

The authors, independently, developed an alternative exponential fitting function for the following reasons: (a) the plot of peak vibration amplitude versus the mass–damping parameter on a linear scale looks like an exponentially decaying function and (b) since the damping force is proportional to cylinder velocity, it should take very large (tending towards infinite) amount of damping to completely suppress the VIV. The following general exponential fitting function was conceptualized to take into account the expected asymptotic behaviour

$$A^* = A_0^* \exp\left(\sum_{i=1}^{n} C_i\alpha^i\right), \tag{7}$$
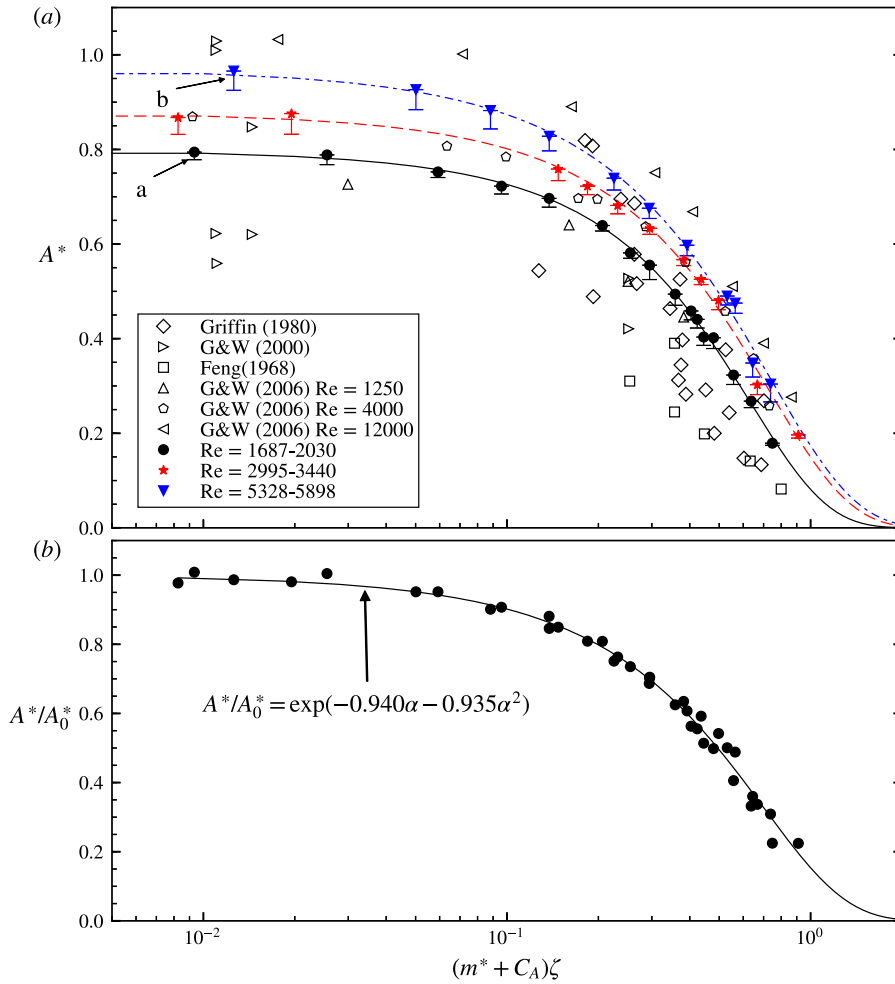
Fig. 15. (a) Griffin plot, showing the comparison of our results for three Re ranges with the published data. The error bars represent the difference between the A^* and A^*_{10} values and signify the variation in the vibration amplitude over time. G & W stands for Govardhan and Williamson. (b) The collapse of all the data points from our experiments onto a single curve by considering the effect of Reynolds number.

Table 2
Coefficients of the exponential fit, obtained by least-squares fitting method, for the peak vibration amplitude data shown in Fig. 15(a).

Set	Re range	A^*_0	C_0	C_1
1	1687–2030	0.798	−0.802	−1.483
2	2995–3440	0.878	−0.812	−0.959
3	5328–5898	0.970	−0.966	−0.755

where C_i are constants determined based on a least-squares fit. A second-order form ($n = 2$) was found to give an excellent fit. Fig. 14 is taken from Govardhan and Williamson (2006) and shows comparison of three fitting functions: quadratic fitting, the fitting proposed by Sarpkaya (1978), and Eq. (7) with $n = 2$. Both the quadratic and exponential fitting functions overlap over the available data range shown by the circular markers. As noted by Govardhan and Williamson (2006), the quadratic fit does not behave nicely in the high mass–damping region where it first predicts a negative peak vibration amplitude and then an increase in peak vibration amplitude with mass–damping. The exponential fit, on the other hand, predicts a slowly decaying peak vibration amplitude with mass–damping. The fitting proposed by Sarpkaya (1978) also shares the property of requiring an infinite amount of damping to completely suppress the VIV but it is less accurate in fitting the available data (see appendix B of Govardhan and Williamson (2006)).

The local peaks of the cylinder displacement were detected and their maximum was labelled as the maximum vibration amplitude at the corresponding combination of the reduced velocity and mass–damping. The maximum vibration amplitude is important from the structural engineering point of view. However, the vibration amplitude can vary from one cycle to
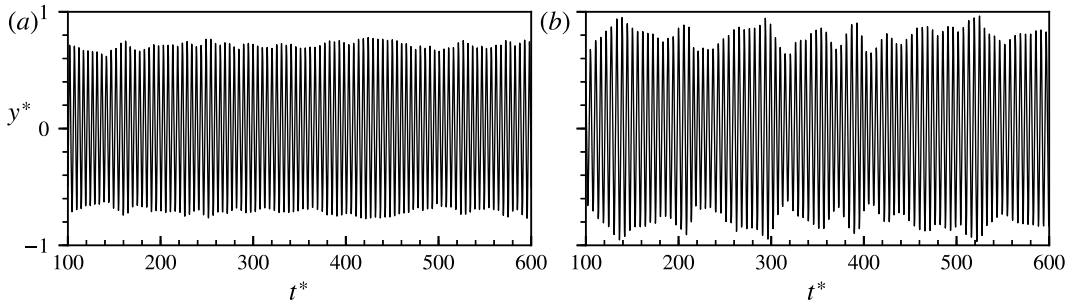
Fig. 16. The non-dimensional cylinder displacement versus non-dimensional time plots illustrating the variation of the displacement amplitude with time. The subplots (a) and (b) correspond to the data points shown in Fig. 15(a). A large standard deviation in the vibration amplitude is an indication of a larger variation in its values as seen in the subplot (b).

Table 3
Root mean squared error of three fitting functions for the peak vibration amplitude data shown in Fig. 15(a).

Set	Re range	RMS error		
		Eq. (7) with $n = 2$	Quadratic fit by Govardhan and Williamson (2006)	Fitting by Sarpkaya (1978)
1	1687–2030	0.023	0.017	0.129
2	2995–3440	0.036	0.048	0.128
3	5328–5898	0.040	0.035	0.071

another (see Fig. 8) and its maximum value may not repeat at several instants. Therefore, there is an uncertainty in the maximum vibration amplitude. Another possibility is to sort the local peaks in descending order and then take the mean of the few top values. In the present work, mean of top 10% values (A^*_{10}) is used for this approach. Notice that, for any mass–damping value, the maximum vibration amplitude attains a global maximum value at some optimal reduced velocity. This global maximum is referred to as the peak vibration amplitude (A^*) in the present work. The peak vibration amplitude of the cylinder as a function of mass–damping, for three sets of experiments reported in Table 1, is plotted in Fig. 15(a). The exponential fitting function, Eq. (7) with $n = 2$, is used to connect the data points. The coefficients of the fit are listed in Table 2. The error bars in Fig. 15(a) represent $A^* - A^*_{10}$ and provide a measure of degree of uncertainty in the peak vibration amplitude. For a harmonic signal, A^* and A^*_{10} values will be identical and therefore the error will be zero. A larger error value signifies a larger variation in the vibration amplitude over time. For example, consider the time histories of the cylinder displacement shown in Fig. 16(a) and 16(b) which corresponds to the data points labelled as *a* and *b*, respectively, in Fig. 15(a). Clearly, a small error implies a smaller variation in the vibration amplitude with time.

The peak vibration amplitude of the circular cylinder is seen to increase with Reynolds number. This could be related to the decrease in the viscous component of the lift force acting on the cylinder. Table 3 shows the root mean square (RMS) error for three types of fitting used in Fig. 14 at three different Reynolds numbers. The RMS error is defined as

$$E_{rms} = \sqrt{\frac{1}{N} \sum_{i=1}^{N} \left(\frac{A^* - A^*_{fit}}{A^*} \right)^2}, \tag{8}$$

where A^* is the measured vibration amplitude, A^*_{fit} is the vibration amplitude obtained from fit and N is the total number of dataset points. Both exponential and quadratic fitting give similar RMS errors while the fit proposed by Sarpkaya has a larger error. Therefore, the exponential fit in Eq. (7) performs as good as the quadratic fitting function while having a better basis, given the physical behaviour at higher mass–damping values.

Interestingly, the peak vibration amplitude occurs at different reduced velocities at different damping values. In general, the optimal reduced velocity corresponding to peak vibration amplitude increases with damping because the damped natural frequency of a linear spring–mass system is known to be smaller than the undamped one. Therefore, there is a small variation in Reynolds number corresponding to each data point in Fig. 15(a) for each set of experiments. The range of variation in Re is also shown in Table 3. To account for the Reynolds number effect, the undamped peak vibration amplitude in Eq. (7) is expressed as $A^*_0 = \log_{10}(D\text{Re}^E)$ where D and E are constants. Note that this is the same fit that was proposed by Govardhan and Williamson (2006). The four constants in the modified form of Eq. (7) are then determined by a least-squares fit of all the data from three sets of experiments in Fig. 15(a). The set of values of constants obtained is $(D, E, C_1, C_2) = (0.402, 0.366, -0.940, -0.935)$. Once the constants D and E are known, the effect of Re in the Griffin plot can be eliminated by dividing the individual A^*_0 data in Fig. 15(a) by the A^*_0 corresponding to the Re value at that data point. The resulting Griffin plot is shown in Fig. 15(b), which shows a strong collapse of the peak vibration amplitude, normalized by its undamped value, on a single curve. Therefore, as an alternative to the fit proposed by Govardhan and Williamson (2006), the following equation can be used to predict the peak vibration amplitude (A^*) of a circular cylinder undergoing VIV
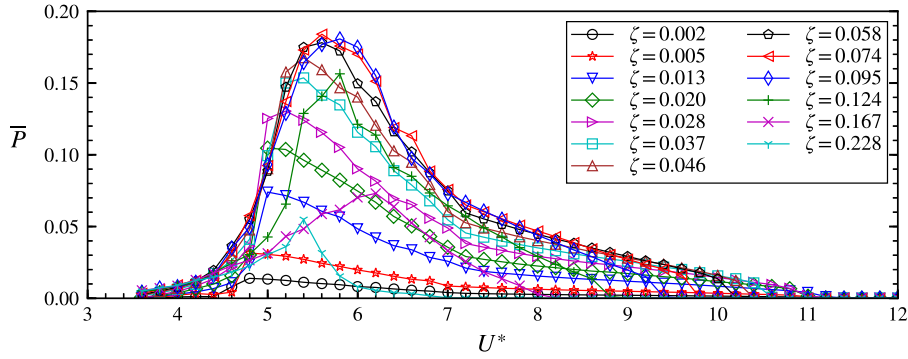
Fig. 17. The average extracted power versus reduced velocity for various values of damping ratios.

as a function of mass–damping (α) and Reynolds number (at least over the range of Re considered in this study)

$$A^* = \log_{10}\left(0.402\text{Re}^{0.366}\right)\exp\left(-0.940\alpha - 0.935\alpha^2\right). \tag{9}$$

3.5. Power extraction

The fluctuating lift force acting on the cylinder, due to vortex shedding, causes the cylinder to vibrate. The vibration of the cylinder suggests a way to extract power from the fluid flow. Any power extraction process can be modelled as the addition of damping to the system. Usually, the damping coefficient for the power-harvesting device is modelled as a constant. In Soti et al. (2017), it was shown that a constant damping ratio model predicts the same average power that will be extracted by a more realistic electromagnetic power extraction device where the damping is far from constant. In the present experiments, different damping values were introduced to the system and then the extracted power was calculated by using the observed cylinder displacement and the preset value of damping introduced to the system. If the cylinder displacement at any instant is given by $y(t)$, then the instantaneous non-dimensional power extracted by the damper is $P(t) = c\dot{y}(t)^2/(\frac{1}{2}\rho U^3 DL)$, which can also be written as

$$P(t) = 2\pi^2 f_n^* m^* \zeta \dot{y}^{*2}, \tag{10}$$

where $f_n^* = f_n D/U$ and $y^* = y/D$ are the non-dimensional natural frequency in a vacuum and the displacement of the cylinder, respectively. Since the cylinder undergoes a periodic motion, the average extracted power over an oscillation cycle can be defined as $\overline{P} = \frac{1}{T}\int_0^T P(t)dt$ where T is the oscillation period. The cylinder displacement can be approximated as $y^* = A_y^* \sin(2\pi f_y f_N^* t^*)$ where A_y^*, f_y and f_N^* are non-dimensional displacement amplitude, normalized vibration frequency and non-dimensional natural frequency of the cylinder in water, respectively. Using this approximation, the average power can be simplified to

$$\overline{P} = 4\pi^4 f_n^{*2} f_y^2 m^* \zeta \left(\frac{A_y^*}{U^*}\right)^2. \tag{11}$$

The average power varies from one vibration cycle to another because of the variation in vibration amplitude. In the present experiments, the average power was calculated over many ($\approx$100) vibration cycles. The average extracted power as a function of reduced velocity is shown in Fig. 17 for various damping values for set 2. At any damping value, an optimal reduced velocity exists at which $\overline{P}$ is maximum. Since the vibration amplitude and thereby the cylinder velocity attains its maximum in the upper branch, it is expected that $\overline{P}$ will be maximum in the upper branch.

In general, the value of optimal U^* at which the average power is maximum may not be the same as that of the maximum vibration amplitude. In the present experiments, these optimal U^* values are found to differ by 0.5 for set 1 and 1.0 for set 2 and set 3 at the minimum damping. This indicates that the difference in the optimal U^* could be a function of Reynolds number. At high damping, the difference is always zero. The difference decreases with the increasing damping in a gradual manner. Notice that there is a uncertainty of $\pm$0.2 in the difference values. The normalized vibration frequency is close to 1.0 in the upper branch where the average power is maximum. Since the vibration amplitude varies from one vibration cycle to another, the maximum average power is approximated as $\overline{P}_m = C_0\alpha\overline{A^*}^2$, where C_0 is a constant and $\overline{A^*}$ is the peak mean vibration amplitude of the cylinder. Assuming that the peak mean vibration amplitude can be related to the mass–damping using a function similar to Eq. (7), the maximum average power is approximated as

$$\overline{P}_m = C_3\alpha\exp\left(C_1\alpha + C_2\alpha^2\right), \tag{12}$$

Table 4
Coefficients of the exponential fit, obtained by least-squares fitting method, for the maximum average power.

Set	Re range	C_3	C_1	C_2
1	1560–1998	1.591	−3.624	−1.739
2	2662–3440	1.512	−2.222	−2.246
3	4757–5708	1.581	−1.922	−2.637
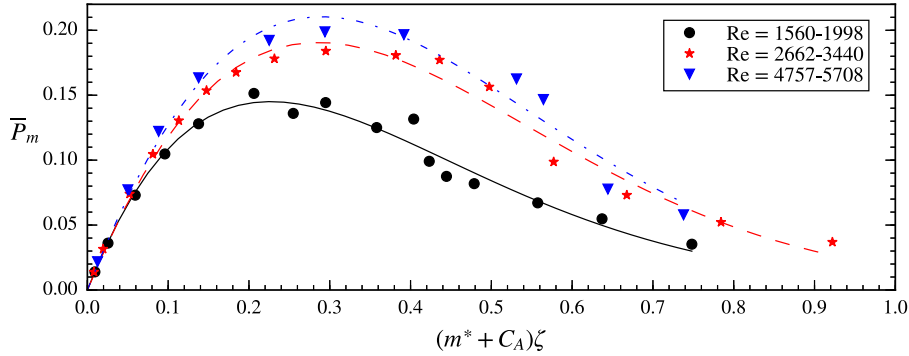
Fig. 18. The maximum average extracted power versus damping ratio for three Reynolds number ranges given in Table 1.

where $C_3 = C_0(\overline{A_0^*})^2$ and $\overline{A_0^*}$ is the peak mean vibration amplitude at zero damping. Notice that n is taken as 2 in Eq. (12) as the use of only two terms inside the exponential was found to be sufficient for accurate fitting in Section 3.4.

The maximum average power $(\overline{P}_m)$ obtained from the present experiments is plotted in Fig. 18 for three ranges of Reynolds number. Notice that the Re range in Fig. 18 differs from that in Fig. 15(a) because the optimal values of U^* for average power and peak amplitude are different. The data is fitted to Eq. (12) using the least-squares method. The constants of Eq. (12) obtained by the least-squares fit are listed in Table 4. From Fig. 18, it is seen that there is also an optimal damping at which $\overline{P}_{max}$ is maximum. The existence of an optimal damping can be explained by the following argument. The extracted power will be zero at zero damping. On the other hand, the extracted power will also be zero at very large damping due to complete suppression of the cylinder vibration. Therefore, as the damping is increased from zero, the extracted power should first increase with damping then reach a maximum for some optimal damping before decreasing back to zero. Since the vibration amplitude increases with Reynolds number, the extracted power is expected to increase too. Fig. 18 also shows the effect of Re on extracted power. As expected, the extracted power increases with Reynolds number. The value of optimal damping also increases with Reynolds number. In the present work, the maximum value of $\overline{P}_m$ was found to be close to 0.151, 0.184 and 0.200 for Re $\approx$ 1747, 3107 and 5328, respectively. Barrero-Gil et al. (2012), using forced vibration data, calculated the maximum efficiency values close to 0.18 and 0.24 for Re = 3800 and 10,000, respectively. Grouthier et al. (2014), using a wake-oscillator model, calculated the value of maximum flow power extraction efficiency to be 0.23. Notice that both of the previous studies were based on some form of modelling while the present results are from direct measurement. Bernitsas et al. (2008) measured the power extraction efficiency of their VIVACE device to be equal to 0.22 for Re $\approx$ 93 000, though they did not optimize this value. Lee and Bernitsas (2011) experimentally found the maximum efficiency of VIVACE device to be 0.33 for Re $\approx$ 75 000. Soti et al. (2017), through numerical simulations, calculated the power extraction efficiency to be 0.10, 0.13 and 0.145 at Re = 100, 150 and 200, respectively. The present work provides power extraction data in the lower ranges of Reynolds number where there is a lack of information in the literature. It also demonstrates the superiority of VIV over other techniques, such as turbines and watermills, in extracting flow energy at much smaller flow velocities.

Assuming that the peak mean vibration amplitude at zero damping follows a logarithmic relationship with Reynolds number similar to the one used in Section 3.4, the average power as a function of Reynolds number and mass–damping is written as

$$\overline{P}_m = \left[\log_{10}\left(0.252\mathrm{Re}^{0.538}\right)\right]^2 \alpha \exp\left(-2.882\alpha - 1.779\alpha^2\right). \tag{13}$$

The coefficients in Eq. (13) were obtained by using a least-squares fit on the all data points in Fig. 18.

4. Conclusions

The effects of damping on the vortex-induced vibration of a circular cylinder of mass ratio 3.0 were studied experimentally in a water channel for Reynolds number ranging from 1200 to 11,000. An eddy-current-based passive damping mechanism was used to apply various damping levels to the system. The cylinder vibration response and the fluid forces were recorded

as a function of the reduced velocity over a range of damping values. The flow power extracted by the damper was also calculated.

The typical three-branch VIV response (the initial, upper and lower branches) is observed at low damping values. The transition from one branch to another occurs with a jump in the vibration amplitude. These jumps in amplitude response get smeared out as the damping is increased. The frequency response also shows jumps at the boundaries of the branches at low damping but these jumps disappear at higher damping. However, there are the following similarities between frequency responses at low and high damping: there is a region of reduced velocity at higher damping similar to (a) the initial branch where the vibration frequency matches with the vortex shedding frequency for a stationary circular cylinder; (b) the upper branch where the vibration frequency is close to the natural frequency of cylinder and increases moderately with the reduced velocity; and (c) the lower branch where the vibration frequency stays constant. Therefore, it is reasonable to also label these regions as the initial, upper and lower branches, respectively, for higher damping cases. Based on the above finding, the existence of the upper branch was found to continue down to $A^* \approx 0.2D$. The frequency of vibration decreases by a little with damping in all of these regions since the damped natural frequency is smaller than the undamped one. The amplitude response decreases with increasing damping due to an increase in the dissipation of the kinetic energy of cylinder by the damper. As the damping is increased, all branches are seen to shrink in terms of the range of reduced velocity. Consequently, the synchronization region also shrinks with increasing damping.

The lift force also shows a monotonic decrease with increasing damping. Since the power dissipation is proportional to the sine of the phase difference between the lift and displacement signals, the total phase remains close to 0° and 180° for low damping. As the damping is increased, the total phase tends to vary in a continuous fashion with reduced velocity.

The effect of damping on the peak vibration amplitude is quantified by plotting it against the product of mass and damping ratios (called mass–damping) in the *Griffin plot*. The peak amplitude data, obtained by varying the damping and keeping the Reynolds number fixed, shows a smooth variation with mass–damping. Three sets of experiments with different Reynolds number ranges were conducted to account for the Reynolds number effects. The experiments agree with the finding of Govardhan and Williamson (2006) that the scatter in previously reported Griffin plots is due to the Reynolds number variation. An exponential fitting function is proposed that fits the peak amplitude data with excellent accuracy and shows a monotonic decay of peak amplitude at higher mass–damping.

The amount of power dissipated by the damper was also calculated and was regarded as the power that can be extracted from the flow through VIV of the cylinder. At any damping value, there is an optimal reduced velocity for extracting maximum power. Also, there is an optimal damping value at any reduced velocity at which the extracted power is maximum. Therefore, there is an optimal combination of damping and reduced velocity where the extracted power attains its global maximum value. The vibration amplitude and hence the extracted power is seen to increase with Reynolds number. The maximum average extracted power was found to be close to 0.151, 0.184 and 0.200 for Re $\approx$ 1747, 3107 and 5328, respectively. The fit for the peak vibration amplitude was extended to express the average extracted power as a function of Reynolds number and mass–damping.

References

Barrero-Gil, A., Pindado, S., Avila, S., 2012. Extracting energy from vortex-induced vibrations: a parametric study. Appl. Math. Model. 36 (7), 3153–3160.

Bearman, P., 2011. Circular cylinder wakes and vortex-induced vibrations. J. Fluids Struct. 27 (5), 648–658.

Bernitsas, M.M., Raghavan, K., Ben-Simon, Y., Garcia, E., 2008. Vivace (Vortex Induced Vibration Aquatic Clean Energy): A new concept in generation of clean and renewable energy from fluid flow. J. Offshore Mech. Arct. Eng. 130 (4), 041101.

Blevins, R.D., Coughran, C.S., 2009. Experimental investigation of vortex-induced vibration in one and two dimensions with variable mass, damping, and Reynolds number. J. Fluids Eng. 131 (10), 101202.

Donoso, G., Ladera, C., Martin, P., 2009. Magnet fall inside a conductive pipe: motion and the role of the pipe wall thickness. Eur. J. Phys. 30 (4), 855.

Feng, C., 1968. The Measurement of Vortex Induced Effects in Flow Past Stationary and Oscillating Circular and D-Section Cylinders (Master thesis), University of British Columbia, Canada.

Gabbai, R., Benaroya, H., 2005. An overview of modeling and experiments of vortex-induced vibration of circular cylinders. J. Sound Vib. 282 (3), 575–616.

Govardhan, R., Williamson, C.H.K., 2000. Modes of vortex formation and frequency response of a freely vibrating cylinder. J. Fluid Mech. 420, 85–130.

Govardhan, R., Williamson, C.H.K., 2006. Defining the modified Griffin plot in vortex-induced vibration: revealing the effect of Reynolds number using controlled damping. J. Fluid Mech. 561, 147–180.

Griffin, O., 1980. Vortex-excited cross-flow vibrations of a single cylindrical tube. J. Press. Vessel Technol. 102 (2), 158–166.

Grouthier, C., Michelin, S., Bourguet, R., Modarres-Sadeghi, Y., De Langre, E., 2014. On the efficiency of energy harvesting using vortex-induced vibrations of cables. J. Fluids Struct. 49, 427–440.

Jauvtis, N., Williamson, C.H.K., 2004. The effect of two degrees of freedom on vortex-induced vibration at low mass and damping. J. Fluid Mech. 509, 23–62.

Khalak, A., Williamson, C.H.K., 1997. Fluid forces and dynamics of a hydroelastic structure with very low mass and damping. J. Fluids Struct. 11 (8), 973–982.

Khalak, A., Williamson, C.H.K., 1999. Motions, forces and mode transitions in vortex-induced vibrations at low mass-damping. J. Fluids Struct. 13 (7–8), 813–851.

Klamo, J.T., 2009. The application of controlled variable magnetic eddy current damping to the study of vortex-induced vibrations. Exp. Fluids 47 (2), 357–367.

Klamo, J., Leonard, A., Roshko, A., 2005. On the maximum amplitude for a freely vibrating cylinder in cross-flow. J. Fluids Struct. 21 (4), 429–434.

Klamo, J., Leonard, A., Roshko, A., 2006. The effects of damping on the amplitude and frequency response of a freely vibrating cylinder in cross-flow. J. Fluids Struct. 22 (6), 845–856.

Lee, J., Bernitsas, M., 2011. High-damping, high-Reynolds VIV tests for energy harnessing using the VIVACE converter. Ocean Eng. 38 (16), 1697–1712.

Leontini, J.S., Thompson, M.C., Hourigan, K., 2006. The beginning of branching behaviour of vortex-induced vibration during two-dimensional flow. J. Fluids Struct. 22 (6), 857–864.

Morse, T., Williamson, C., 2009. Fluid forcing, wake modes, and transitions for a cylinder undergoing controlled oscillations. J. Fluids Struct. 25 (4), 697–712.

Raghavan, K., Bernitsas, M.M., Maroulis, D., 2009. Effect of bottom boundary on VIV for energy harnessing at $8 \times 10^3 <$ Re $< 1.5 \times 10^5$. J. Offshore Mech. Arct. Eng. 131 (3), 031102.

Sareen, A., Zhao, J., Lo Jacono, D., Sheridan, J., Hourigan, K., Thompson, M.C., 2018. Vortex-induced vibration of a rotating sphere. J. Fluid Mech. 837, 258–292.

Sarpkaya, T., 1978. Fluid forces on oscillating cylinders. ASCE J. Waterway Port Coast. Ocean Div. 104, 275–290.

Sarpkaya, T., 2004. A critical review of the intrinsic nature of vortex-induced vibrations. J. Fluids Struct. 19 (4), 389–447.

Schieber, D., 1975. Optimal dimensions of rectangular electromagnet for braking purposes. IEEE Trans. Magn. 11 (3), 948–952.

Soti, A.K., Thompson, M.C., Sheridan, J., Bhardwaj, R., 2017. Harnessing electrical power from vortex-induced vibration of a circular cylinder. J. Fluids Struct. 70, 360–373.

Williamson, C.H.K., Govardhan, R., 2004. Vortex-induced vibrations. Annu. Rev. Fluid Mech. 36, 413–455.

Williamson, C.H.K., Roshko, A., 1988. Vortex formation in the wake of an oscillating cylinder. J. Fluids Struct. 2 (4), 355–381.

Wong, K.W.L., Zhao, J., Lo Jacono, D., Thompson, M.C., Sheridan, J., 2017. Experimental investigation of flow-induced vibration of a rotating circular cylinder. J. Fluid Mech. 829, 486–511.

Zhao, J., Leontini, J.S., Lo Jacono, D., Sheridan, J., 2014a. Chaotic vortex induced vibrations. Phys. Fluids 26 (12), 121702.

Zhao, J., Leontini, J.S., Lo Jacono, D., Sheridan, J., 2014b. Fluid–structure interaction of a square cylinder at different angles of attack. J. Fluid Mech. 747, 688–721.